Online appendix: Additional analysis and model results

This appendix comprises three main sections. The first provides additional analysis for our numerical model, the second provides additional results from our analytical model, and the third summarizes additional simulations we have performed to test the role of different nondimensional parameters on the flow behavior.

1. Additional analysis for the numerical model

1.1. *Verification of the advection-diffusion equation used in the miscible simulations*

For the simulations of miscible fluids, we use a finite difference scheme to solve the advection-diffusion equation (2.21) for concentration. In the spatial discretization, we use a fifth-order weighted-essentially-non-oscillatory scheme to represent the advection term and a second-order central-difference scheme for the diffusion term. In the temporal discretization, we use a third-order, total-variation-diminishing Runge-Kutta scheme. To verify the accuracy of our strategy, we compare our numerical solution to a one-dimensional advection-diffusion problem with its analytical solution.

In this benchmark, we solve the equation

$$\begin{aligned} \frac{\partial c(t,x)}{\partial t} &= k\frac{\partial^2 c(t,x)}{\partial x^2} + v\frac{\partial c(t,x)}{\partial x} \ , \\ t &> 0 \ , \\ 0 &< x < 10 \ , \end{aligned} \tag{1.1}$$

where $k = 0.5$ is the diffusivity and $v = 0.5$ is the imposed advection speed. We specify the boundary conditions

$$\begin{aligned} c(t,0) &= 0 \ , \\ c(t,10) &= 1 \ . \end{aligned} \tag{1.2}$$

The initial conditions are

$$c(0,x) = \begin{cases} 0 & 0 \leqslant x < 10 \\ 1 & x = 10 \end{cases} \ . \tag{1.3}$$

The equation can be solved analytically using separation of variables. The analytical solution is

$$c(t,x) = e^{-(\frac{v^2 t}{4k} + \frac{vz}{2k})} u(t,x) \ , \tag{1.4}$$

where

$$\begin{aligned} u(t,x) = &\frac{x}{10} e^{(\frac{v^2 t}{4k} + \frac{vz}{2k})} \\ &+ \sum_{n=1}^{\infty} \left(\frac{2(-1)^n v^2 e^{-k\lambda_n t + \frac{10v}{2k}} (e^{k\lambda_n t + \frac{tv^2}{4k}} - 1)}{n\pi(4k^2\lambda_n + v^2)} + \frac{2}{10} \frac{(-1)^n e^{\frac{10v}{2k}}}{\sqrt{\lambda_n}} e^{-k\lambda_n t} \right) \sin(\sqrt{\lambda_n} x) \ , \end{aligned} \tag{1.5}$$

and

$$\lambda_n = (\frac{n\pi}{10})^2 \ \text{ for } \ n = 1, 2, ... \tag{1.6}$$

We compare the numerical evolution of c to the analytical solution in figure S1 (A), with a spatial grid of 161 cells and a temporal step of $\Delta t = 2.4 \times 10^{-4}$. The numerical solution reaches a good agreement with the analytical solution. In figure S1 (B), we show a convergence test for the numerical scheme demonstrating second-order convergence in space at $\Delta t = 2.4 \times 10^{-4}$.

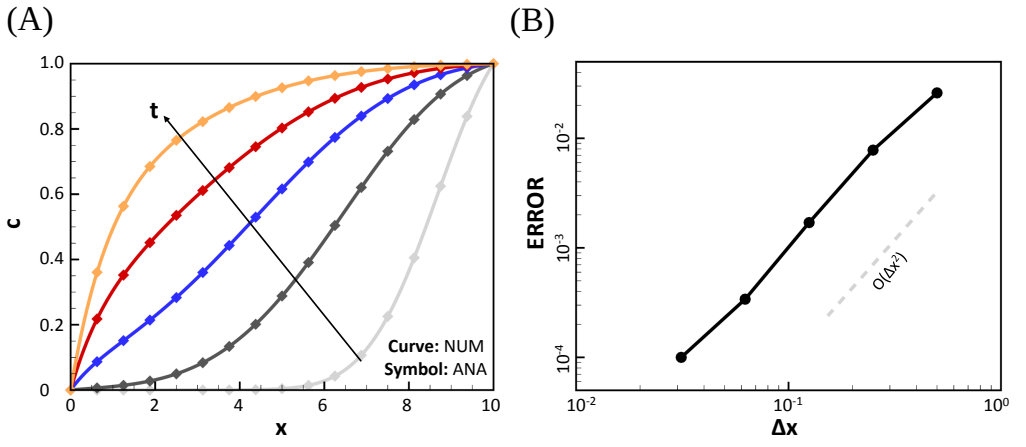

Figure S1: (A) Evolution of numerical (curve) and analytical (symbol) c; (B) Convergence of the error for spatial resolution, second-order accuracy is obtained.

1.2. *Convergence test and adaptive grid refinement*

In figure S2, we reproduce experiment #5 to evaluate whether the simulation converges as the spatial (figure S2A) and temporal (figure S2B) resolution are increased. The computation assumes two miscible fluids with low diffusivity (i.e., $D = 10^{-10}\mathrm{m}^2/\mathrm{s}$). We test convergence by comparing the numerical rise speed to the corresponding analytical solution despite the fact that the analytical solution strictly applies only to two immiscible fluids. The numerical rise speed is taken along a horizontal cross section in an area of well-developed flow. Both convergence rates are first order. To increase the accuracy of the numerical model efficiently, we apply an adaptive grid refinement strategy. In the simulation of both immiscible and miscible flow, our grid hierarchy comprises two levels. Level 1 is a fixed, coarse grid that defines the whole computational domain. Level 2 is an adaptively generated, fine grid that overlays the coarse level. The fine grid covers the whole liquid-liquid interface to accurately simulate the evolution of flow regimes. As the bidirectional flow develops and the interface extends through the domain, the area covered by the fine grid is increased as well. Compared to a simulation using the finer grid resolution over the entire computational domain, this adaptive grid refinement strategy obtains the same high accuracy, but saves more than 50% of the computational expense. More details of our adaptive grid refinement strategy are discussed in Qin & Suckale (2017).

1.3. *Comparison of the average rise speed to the frontal rise speed*

In their analogue experiments, Stevenson & Blake (1998) calculated the Ps number using the frontal rise speed of the ascending liquid. Our analytical model assumes that core-annular flow is at steady state, which is not compatible with a propagating front. To compute Ps with our analytical model, we use the average rise speed, which we define as the average of the vertical velocity component in the lateral direction across the ascending liquid in the core, and use the experimental Ps numbers to estimate the core radius. Figure S3 compares the two velocity measures for experiment #8. Figure S3(B) shows that both frontal rise speed and average rise velocity reach a similar steady state after an initial spin-up. We also compare the two rise-speed estimates for other

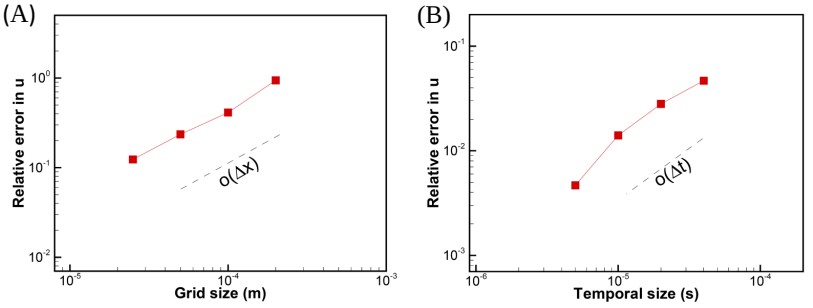

Figure S2: Convergence tests for the relative L2 error of numerical rise speed. Convergence of the relative error is first order for both spatial (**A**) and temporal (**B**) resolution.

experiments and find that the difference is always small ($< 5\%$) and will decrease with spatial and temporal resolution.

1.4. *Comparison of the linear dependence of viscosity on concentration to a potential nonlinear dependence*

Several numerical studies of bidirectional flow in miscible fluids have applied a nonlinear dependence of viscosity on concentration instead of a linear one, which we use in the present study. For example, Meiburg *et al.* (2004) defined an exponential relationship between viscosity and concentration as

$$\mu = \mu_a e^{ln\frac{\mu_d}{\mu_a}c} \ . \tag{1.7}$$

In figure S4, we compare a simulation with a linear viscosity profile to one with an exponential viscosity profile for experiment #5. In both simulations, we use a linear density profile. We find that the exponential viscosity profile is associated with a notably different speed profile (S4C) as compared to the linear case. The exponential viscosity profile entails an increased downward velocity in the buoyant fluid close to the fluid-fluid interface. Because the density profile is linear, the buoyancy force changes linearly across the interface, whereas the viscous resistance changes exponentially (figure S4D). This means that there is a thin boundary layer of relatively heavy fluid that has relatively low viscosity and is therefore actively sinking, as indicated by the downward-oriented peak in the speed apparent in figure S4C.

2. Additional results from the analytical model

2.1. *2D formulation*

The analytical model for a general tube geometry in 3D, described in detail in the main article, can also be formulated in 2D. We use the 2D formulation of the analytical model to compute influx and outflux boundary conditions for our 2D numerical simulations (e.g., figure 11 in the main article). In the 2D case, the nondimensional vertical speed in the two fluids is

$$u_d(y) = \frac{P}{2}\left(y^2 - 1\right) - \delta\cos\alpha(y-1), \quad y \in [\delta, 1] \tag{2.1}$$

$$u_a(y) = \mathrm{M}\frac{P - \cos\alpha}{2}\left(y^2 - \delta^2\right) + \frac{P}{2}\left(\delta^2 - 1\right) - \delta\cos\alpha\left(\delta - 1\right), \quad y \in [0, \delta], \tag{2.2}$$

where $0 \leqslant y \leqslant 1$ is the Cartesian direction perpendicular to the side boundaries and δ is the half-thickness of the ascending fluid. We will later use these expressions as boundary

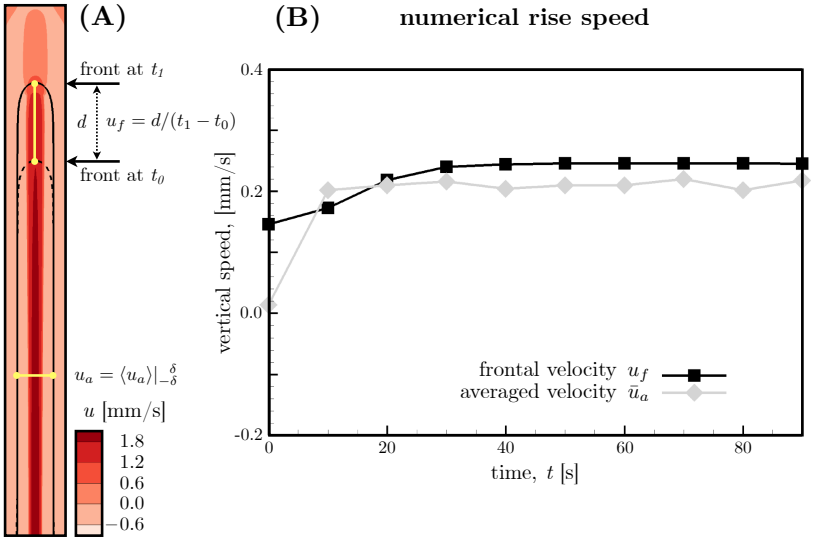

Figure S3: Illustration of two numerical metrics for the rise speed in our virtual reproduction of experiment #8. **(A)** The frontal rise speed, u_f, is computed by measuring the distance that the front of the ascending liquid has covered in a given time interval; the average rise speed, $\bar{u}_a$ is defined by averaging the vertical velocity of the ascending liquid along a horizontal cross section taken in an area of fully developed bidirectional flow. **(B)** Both u_f and $\bar{u}_a$ reach similar steady-state values soon after an initial spin-up period.

conditions to force bidirectional flow in our 2D numerical model (e.g., figure 11 in the main article). Similarly to the 3D case in the main article, the expression for the driving force, P, and the Transport number, Te, are,

$$P(\delta, \alpha, \mathrm{M}) = \delta \frac{3 + \delta^2(2\mathrm{M} - 3)}{2 + 2\delta^3(\mathrm{M} - 1)} \cos\alpha \ , \tag{2.3}$$

$$\mathrm{Te}(\delta, \alpha, \mathrm{M}) = \frac{P}{6}\left(-\delta^3 + 3\delta - 2\right) - \frac{\delta \cos\alpha}{2}\left(-\delta^2 + 2\delta - 1\right) \ . \tag{2.4}$$

2.2. *Viscous dissipation for fully developed laminar concentric core-annular flow*

We compute the dimensionless viscous dissipation for fully developed, laminar, and concentric core-annular flow by integrating the local viscous dissipation rate over the cross-sectional area of the conduit, yielding

$$\Phi = \int_{\delta}^{1} 2\pi r \left(\frac{du_d}{dr}\right)^2 dr + \frac{1}{M}\int_{0}^{\delta} 2\pi r \left(\frac{du_a}{dr}\right)^2 dr = \frac{\mathrm{Te}}{\cos\alpha} \ , \tag{2.5}$$

where u_d and u_a are the velocity profiles of the descending and ascending phase (2.8a and 2.8b), respectively, and the expression for the Transport number Te is given in (2.14). The viscous dissipation is proportional to the dimensionless flux and, in the case of vertical core-annular flow ($\cos\alpha = 1$), we get $\Phi = \mathrm{Te}$.

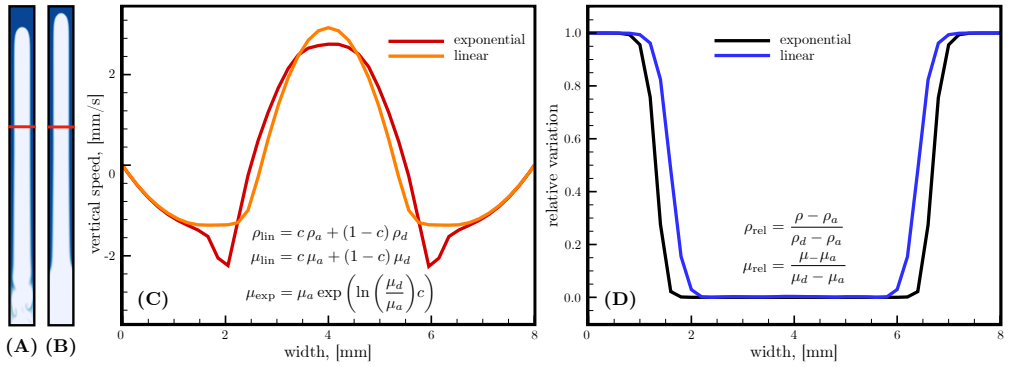

Figure S4: Reproduction of experiment #5 using the linear (A) and exponential (B) dependence of viscosity on concentration. C: Comparison of the numerical velocity profiles between linear (yellow curve) and exponential (red curve) cases on the cross sections represented by the red line in plots A and B. D: Relative density (blue curve) and viscosity (black curve) profiles of the exponential case on the cross section.

2.3. *Estimation of the interfacial speed at different viscosity contrasts*

The direction of motion of the interface determines the phase in which flow reversal occurs. As is evident from our analytical model, the sign of u_i depends sensitively on the driving force, which in turn depends on the viscosity contrast. Figure S5 shows the dependence of the dimensionless interfacial speed u_i on the core radius, δ, and the viscosity contrast, M. Negative interface speeds are associated with flow reversal in the ascending fluid, and positive interface speeds lead to flow reversal in the descending fluid. When the viscosity of the descending phase is significantly higher than that of the ascending core ($M > 10$), flow reversal occurs in the ascending phase across almost the whole range of δ, except for extremely low core radii that are likely dynamically unstable. Conversely, as M decreases, flow reversal begins to shift into the descending phase over a growing range of core radii. If, however, the viscosity ratio is reversed from the experimental setup in Stevenson & Blake (1998), that is if the buoyant fluid is now more viscous than the descending fluid, flow reversal occurs in the descending phase across the entire range of δ.

3. Analysis of the nondimensional regimes and their relevance for the flow behavior

3.1. *Overview of all relevant nondimensional parameters for the reproduced laboratory experiments and additional simulations*

The consideration of both miscible and immiscible fluids at finite and zero Reynolds number implies that there are many relevant, nondimensional parameters, including the Reynolds number, Froude number, Bond number, Péclet number, viscosity contrast, and aspect ratio of the domain. In this section, we provide a list of the nondimensional numbers characterizing both the laboratory experiments and our numerical simulations in table S1. We emphasize that the goal of this section is not to map out the nondimensional parameter space fully, but instead to clearly quantify the nondimensional space explored.

As os evident from table S1, all experiments and simulations are at zero or very low Reynolds number. The emphasis on this regime derives from our goal of understanding volcanic systems, which are characterized by very high fluid viscosities. Consistent with

Table S1: Summary of nondimensional parameters for all simulations, including the laboratory experiment they are based on, miscibility behavior, initial condition (cos or sin fluctuation), density contrast (higher value (H), lower value (L), or the same value as the analogue experiments (O)), Reynolds number (Re), Froude number (Fr), Bond number (Bo), Péclet number (Pe), diffusion coefficient (D), surface tension (σ), the number of the corresponding figures

Case #	Fluids, Initial cond, $\Delta\rho$ misc/imm, cos/sin, H/L/O	Re $\frac{\Delta\rho u R}{\mu_d}$	Fr $\frac{u^2}{gR}$	Bo $\frac{\Delta\rho g R^2}{\sigma}$	Pe $\frac{Ru}{D}$	Figures #
#1	misc. (D=10^{-10},cos,O)	6.0×10^{-8}	3.6×10^{-9}	-	8.4×10^{2}	3,S6
#1	misc. (D=10^{-10},sin,O)	6.0×10^{-8}	3.6×10^{-9}	-	8.4×10^{2}	S6
#2	misc. (D=10^{-10},cos,O)	1.3×10^{-7}	4.0×10^{-9}	-	5.0×10^{2}	3
#3	misc. (D=10^{-10},cos,O)	6.0×10^{-5}	3.4×10^{-7}	-	4.6×10^{3}	3
#4	misc. (D=10^{-10},cos,O)	1.0×10^{-5}	1.6×10^{-7}	-	3.2×10^{3}	3
#5	misc. (D=10^{-10},cos,O)	3.3×10^{-4}	9.4×10^{-6}	-	2.4×10^{4}	3,11,S6,S8
#5	misc. (D=10^{-8},cos,O)	3.2×10^{-4}	9.0×10^{-6}	-	2.3×10^{2}	S8
#5	misc. (D=10^{-7},cos,O)	1.7×10^{-4}	2.3×10^{-6}	-	1.2×10^{1}	S8
#5	misc. (D=10^{-6},cos,O)	NA	NA	-	NA	S8
#5	misc. (D=10^{-10},sin,O)	3.3×10^{-4}	9.4×10^{-6}	-	2.4×10^{4}	S6
#6	misc. (D=10^{-10},cos,O)	7.8×10^{-8}	2.1×10^{-9}	-	3.6×10^{2}	3
#7	misc. (D=10^{-10},cos,O)	1.4×10^{-5}	4.4×10^{-7}	-	1.3×10^{4}	3
#8	misc. (D=10^{-10},cos,O)	1.7×10^{-5}	5.3×10^{-7}	-	1.4×10^{4}	3,4,5,7,S7
#8	misc. (D=10^{-10},cos,L)	4.3×10^{-6}	1.4×10^{-7}	-	7.2×10^{5}	S7
#8	imm. (σ=0mN/m,cos,O)	1.8×10^{-5}	5.3×10^{-7}	∞	-	4,5,S7
#8	imm. (σ=5mN/m,cos,O)	1.8×10^{-5}	5.3×10^{-7}	43	-	S7
#9	misc. (D=10^{-10},cos,H)	5.1×10^{-6}	1.3×10^{-7}	-	1.5×10^{4}	S7
#9	misc. (D=10^{-10},cos,O)	1.1×10^{-6}	3.5×10^{-8}	-	3.6×10^{3}	3,4,7,S7
#9	imm. (σ=0mN/m,cos,O)	1.1×10^{-6}	3.5×10^{-8}	∞	-	4,S7
#9	imm. (σ=5mN/m,cos,O)	1.1×10^{-6}	3.5×10^{-8}	17	-	S7
#10	misc. (D=10^{-10},cos,H)	6.9×10^{-4}	1.2×10^{-5}	-	7.1×10^{4}	S7
#10	misc. (D=10^{-10},cos,O)	1.9×10^{-4}	3.1×10^{-6}	-	3.4×10^{4}	3,4,7,S6,S7,S8
#10	misc. (D=10^{-8},cos,O)	1.5×10^{-4}	2.5×10^{-6}	-	2.6×10^{2}	S8
#10	misc. (D=10^{-7},cos,O)	9.0×10^{-5}	8.0×10^{-7}	-	1.7×10^{1}	S8
#10	misc. (D=10^{-6},cos,O)	NA	NA	-	NA	S7
#10	misc. (D=10^{-10},sin,O)	1.9×10^{-4}	3.1×10^{-6}	-	3.4×10^{4}	S6
#10	imm. (σ=0mN/m,cos,O)	1.9×10^{-4}	3.1×10^{-6}	∞	-	4,S7
#10	imm. (σ=5mN/m,cos,O)	1.9×10^{-4}	3.1×10^{-6}	13	-	S7
#11	misc. (D=10^{-10},cos,O)	3.0×10^{-5}	4.8×10^{-7}	-	5.5×10^{3}	3

that assumption is the small Froude number, which represents the ratio of inertial to gravitational forces. The Bond number quantifies the deformability of the fluid-fluid interface and applies only to immiscible fluids. It is defined as the ratio of the buoyancy force to the surface tension force. Because the interfaces in the experiments and simulations are highly deformable, both nondimensional numbers tend to be high and infinite at zero surface tension. Finally, the Péclet number captures the relative importance of advection to diffusion and applies only in the miscible regime.

3.2. *Impact of the numerical initial condition on the bidirectional flow*

Significant effort in the analysis of bidirectional flow has been devoted to linearized stability analysis and the identification of the fastest-growing wavelengths, in both the

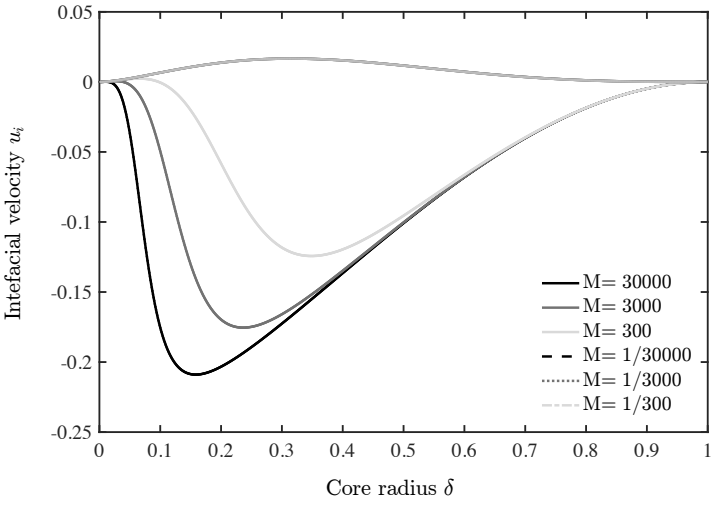

Figure S5: The dimensionless interfacial velocity for the core-annular flow configuration as a function of the core radius δ and the viscosity ratio M. Negative u_i implies flow reversal in the ascending (core) phase and positive u_i implies flow reversal in the descending phase.

immiscible (e.g., Joseph & Renardy 1992) and miscible cases (e.g., Vanaparthy *et al.* 2003). To evaluate whether the nature of the initial perturbation we assume has an effect on the long-term evolution of the flow, we reproduce the analogue experiments with two kinds of perturbations applied to the interface between the two liquids, a sine and a cosine function. The flow regimes at three different viscosity contrasts are shown in figure S6. At high viscosity contrast (experiment #5), steady core-annular flow forms from both initial perturbations. The descending annulus phase, however, is asymmetric when using a sine function initially (A2), in the sense that one side stretches further down than the other, whereas a cosine initial condition leads to a symmetric flow (A3). The degree of asymmetry depends on the magnitude of the initial perturbation. At intermediate viscosity contrast (experiment #1), the simulations with both sine (plot B2) and cosine (plot B3) initial perturbations produce a similar flow regime, where the ascending liquid rises in the center of the tube and the descending liquid breaks into small blobs. At low viscosity contrast (experiment #10), the ascending and descending liquid is approximately symmetric for both initial conditions (figures S6C2-3). According to these results, the shape of the initial perturbation does not determine the flow regime, and will have only a minor effect on the flow symmetry. We also find that the simulations result in similar Ps number independent of their initial perturbation, even though the sine perturbation minimally shortens the time until steady state is reached (see figure S6). Due to the negligible effect of the initial perturbation on the model outcomes, we present only numerical simulations with a cosine initial condition in the main article.

3.3. *Impact of varying only the density contrast as compared to varying both the density and viscosity*

In the analogue experiments of Stevenson & Blake (1998), the density and viscosity ratio vary jointly for each experiment, which makes it difficult to assess the effect of varying only density or only viscosity. In figures S7A1-2, B1-2, and C1-2, we use our numerical model to evaluate the impact of density contrast on miscible flow. In the pairs

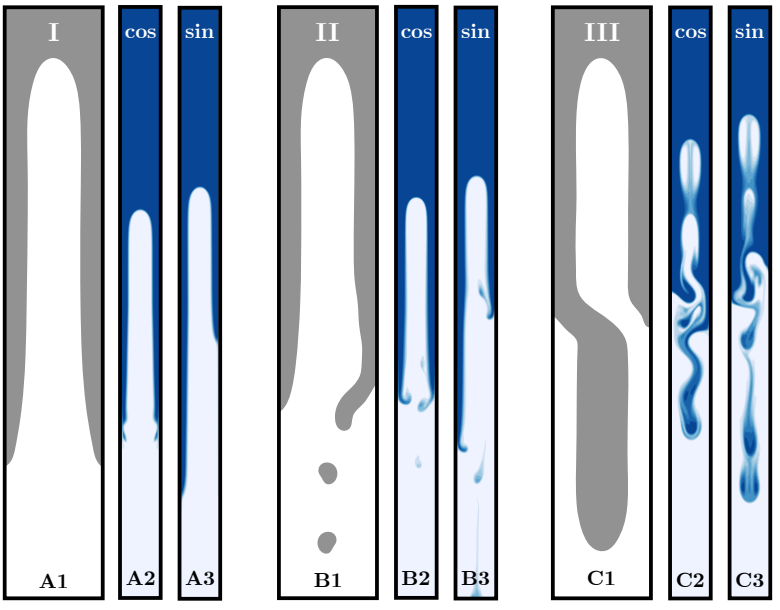

Figure S6: Direct numerical simulations of the three primary flow regimes observed in bidirectional pipe flow for different viscosity contrasts with sine initial perturbation (A2, B2, C2) and cosine initial perturbation (A3, B3, C3) in comparison to sketches (A1, B1, C1) reproduced from the analogue experiments of Stevenson & Blake (1998). All simulation snapshots are taken at $t = 200 \times t_0$.

of A1 and A2, B1 and B2, and C1 and C2, we apply the same viscosity ratio but different density contrasts. The density contrasts of A1, B1, and C1 are twice of A2, B2, and C2. We find that density contrast does not change the flow regime, but that higher density contrast results in higher ascending and descending speeds. This finding is not surprising in light of the fact that the Reynolds number remains very small despite the increase in density contrast. Given the high viscosities, an unreasonably high density contrast would be needed to shift into an inertial flow regime, where the behavior might be different than that shown in figure S7.

3.4. *Analysis of the role of surface tension forces on the stability of bidirectional flow*

We evaluate the impact of surface tension forces in the immiscible flow regime by comparing the flow patterns with zero surface tension (figures S7A3, B3 and C3) to the those with 5 mN/m surface tension (S7A4, B4 and C4). Because the surface tension does not alter the flow regimes, it suppresses interface instabilities, particularly at intermediate viscosity contrast, as is evident from a smoother interface in figure S7B4 as compared to B3. It also changes the morphology of the interface where it is in contact with the wall from flat to blob-like (e.g., see figure S7A4 as compared to A3). This finding is consistent with the theoretical result that surface tension tends to stabilize core-annular flow (e.g., Hickox 1971).

3.5. *Relative importance of advection and diffusion*

In the manuscript (see figure 5), we compare a miscible and an immiscible simulations and conclude that miscibility does not fundamentally alter the three flow regimes observed of Stevenson & Blake (1998). Evidently, this conclusion holds true only as

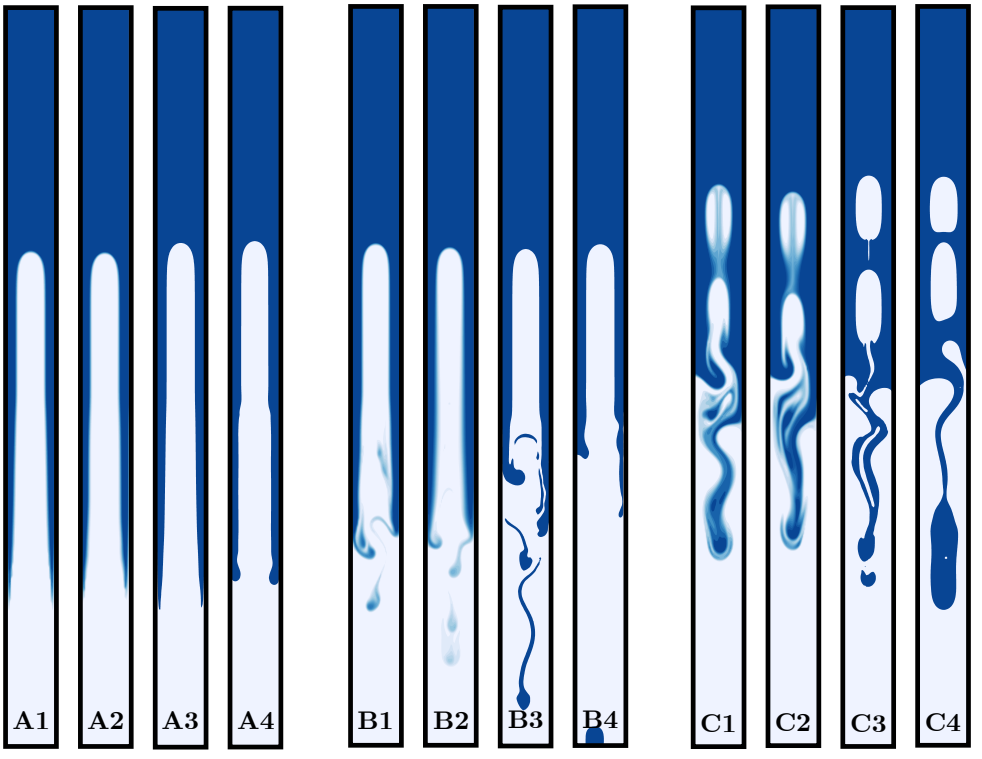

Figure S7: Direct numerical simulations of the three primary flow regimes observed in bidirectional pipe flow for different viscosity contrast. Plots A1-2 (experiment #8), B1-2 (experiment #9), and C1-2 (experiment #10) represent the miscible flow and the density contrasts of A1, B1, and C1 are twice of those of A2, B2, and C2. Plots A3-4 (experiment #8), B3-4 (experiment #9), and C3-4 (experiment #10) represent the immiscible flow. The surface tensions of A3, B3, and C3 are zero, while the surface tensions of A4, B4, and C4 are 5 mN/m. All simulation snapshots are taken at $t = 200 \times \mathrm{t}_0$.

long as advection dominates diffusive processes, or equivalently, if the Péclet number is large enough. As figure S8 demonstrates, we gradually increase the diffusion coefficient, D, to identify the nondimensional regime over which the immiscible flow regimes are maintained in the immiscible context.

Advection dominates the flow regime if the diffusion coefficient is smaller than about $10^{-8}\mathrm{m}^2/\mathrm{s}$, or $\mathrm{Pe} > 10^2$ (see figures S8A1-2 and S8B1-2). In that case, the flow regimes are similar to those observed in the laboratory experiments. As the diffusion coefficient increases, the interface becomes more and more diffuse (e.g., figures S8A3 and B3). At very high diffusivities, $D > 10^{-7}\mathrm{m}^2/\mathrm{s}$, or $\mathrm{Pe} \approx 10$ (see figures S8A4 and B4), the flow is no longer bidirectional but entirely diffusive.

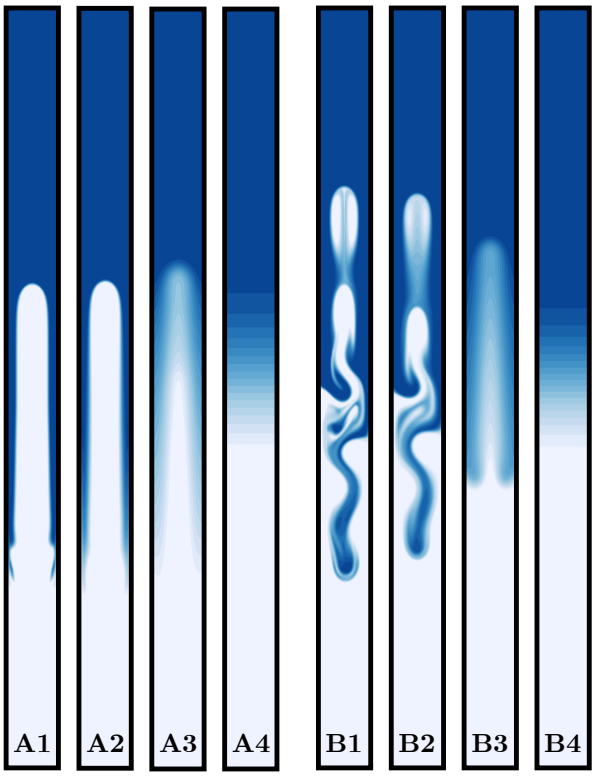

Figure S8: Comparison of the flow regimes with different diffusion coefficients, D. A1-3 are the reproductions of experiment #5, whereas B1-3 are the reproduction of experiment #10. A1 and B1 use $D = 10^{-10}\mathrm{m}^2/\mathrm{s}$; A2 and B2 use $D = 10^{-8}\mathrm{m}^2/\mathrm{s}$; A3 and B3 use $D = 10^{-7}\mathrm{m}^2/\mathrm{s}$; A4 and B4 use $D = 10^{-6}\mathrm{m}^2/\mathrm{s}$. All simulation snapshots are taken at $t = 200{\times}\mathrm{t}_0$.